Néel vector waves in antiferromagnetic CuMnAs excited by surface acoustic waves

M. Waqas Khaliq [1,2,*] Oliver J. Amin,[3] Alberto Hernández-Mínguez,[4] Marc Rovirola,[1,5] Blai Casals,[5,6] Khalid Omari,[7]
Sandra Ruiz-Gómez,[8] Simone Finizio,[9] Richard P. Campion,[3] Kevin W. Edmonds,[3] Vít Novák,[10] Anna Mandziak,[11]
Lucia Aballe,[2] Miguel Angel Niño,[2] Joan Manel Hernàndez,[1,5] Peter Wadley,[3] Ferran Macià,[1,5,†]
and Michael Foerster[2,‡]

[1]*Department of Condensed Matter Physics, University of Barcelona, 08028-Barcelona, Spain*
[2]*ALBA Synchrotron Light Facility, 08290-Cerdanyola del Valles, Barcelona, Spain*
[3]*School of Physics and Astronomy, University of Nottingham, NG7 2RD Nottingham, United Kingdom*
[4]*Paul Drude Institute for Solid State Electronics, 10117-Berlin, Germany*
[5]*Institute of Nanoscience and Nanotechnology (IN2UB), University of Barcelona, 08028-Barcelona, Spain*
[6]*Department of Applied Physics, University of Barcelona, 08028-Barcelona, Spain*
[7]*Department of Electronic Engineering, Royal Holloway, University of London, TW20 0EX-Egham, United Kingdom*
[8]*Max Planck Institute for Chemical Physics of Solids, 01187-Dresden, Germany*
[9]*Swiss Light Source, Paul Scherrer Institute, 5232-Villigen, Switzerland*
[10]*Institute of Physics AS CR, 16253-Prague, Czech Republic*
[11]*SOLARIS National Synchrotron Radiation Centre, 30-392-Kraków, Poland*

Magnetoelastic effects in antiferromagnetic CuMnAs are investigated by applying dynamic strain in the 0.01% range through surface acoustic waves in the GaAs substrate. The magnetic state of the CuMnAs/GaAs is characterized by a multitude of submicron-sized domains, which we image by x-ray magnetic linear dichroism combined with photoemission electron microscopy. Within the explored strain range, CuMnAs shows magnetoelastic effects in the form of Néel vector waves with micrometer wavelength, which corresponds to an averaged overall spin-axis rotation up to 2.4° driven by the time-dependent strain from the surface acoustic wave. Measurements at different temperatures indicate a reduction of the wave amplitude when lowering the temperature. However, no domain wall motion has been detected on the nanosecond timescale.

Antiferromagnets (AFMs) have become a focus of recent research in spintronics, mostly thanks to their potential advantages for future devices. Their low stray fields and robustness versus external magnetic fields are favorable for the further downscaling of memory elements and their high-frequency internal resonances promise higher intrinsic speed limits for operation. However, together with these advantages also challenges arise, for example, related to the readout and mostly the writing process. Magnetic field control, although not completely impossible [1], is impractical due to the field magnitudes required ($\gtrsim 2$ T) in order to overcome exchange energy and modify the magnetization of the two sublattices existing in the AFM. Domain modification by electrical currents has been demonstrated through spin transfer/orbit torque [2] as well as through thermoelastic effects [3]. Specifically for CuMnAs, the manipulation of antiferromagnetic domains in thin films has been studied by means of injecting current pulses [2,4,5] and defects [6]. Other approaches use the transitions to a ferromagnetic (FM) phase, like in FeRh [7], or the coupling with an FM [8], which compromise many of the potential advantages (absence of stray fields, high operation

speed) of AFM materials for usage in a real device. On the other hand, the appearance of closure domainlike features in patterned AFM samples has been attributed to magnetoelastic effects caused by shape-dependent strain [9,10], which suggests that much smaller energies than the exchange energy may be enough to rotate the Néel vector.

Surface acoustic waves (SAWs) are propagating elastic deformations in the upper micrometric layer of a solid. SAWs can be conveniently excited in piezoelectric materials by radiofrequency electrical signals applied to an antenna-like structure named interdigitated transducer (IDT). Typical strain amplitudes achieved under ultrahigh vacuum conditions can reach the range 2×10^{-4} for LiNbO$_3$ in the hundreds of MHz to GHz frequency regime [11]. There is a sizable interaction of SAWs with FM systems in heterostructures, which is driven by the transfer of the space and time-dependent strain state of the underlayer/substrate into the FM overlayer. The interaction is mediated by the magnetoelastic effect and has been investigated by a growing number of groups [12–24] (see review articles [25–27] and references therein). GaAs is a piezoelectric substrate suitable for SAW generation and propagation and allows for epitaxial growth of CuMnAs. This material has substantial applications in optoelectronic devices due to its outstanding photovoltaic properties [28] and robust piezoelectricity [29].

---

*Contact author: mkhaliq@cells.es
†Contact author: ferran.macia@ub.edu
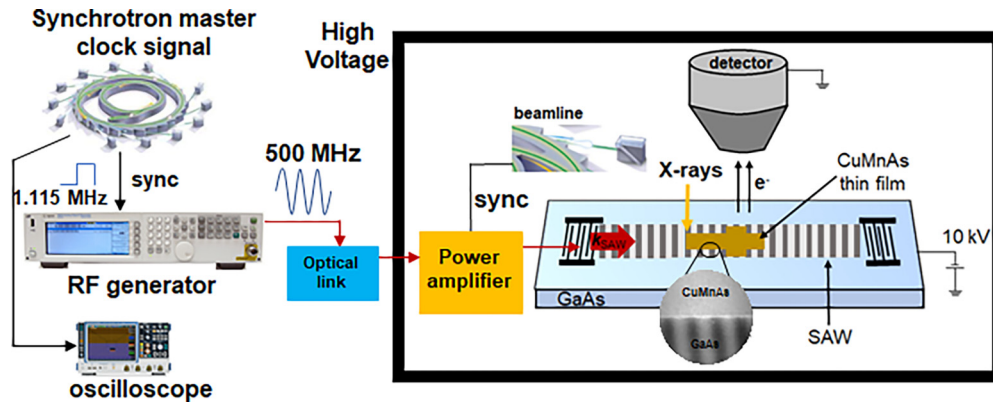‡Contact author: mfoerster@cells.es

FIG. 1. Schematic illustration of the stroboscopic experiment. The CuMnAs thin film is patterned in the acoustic path of the SAW and analyzed in the PEEM microscope. SAWs are generated in the GaAs substrate by applying an electrical signal to the IDTs, which is synchronized with the synchrotron frequency (repetition rate time of the x-ray pulses). The microscope detector (PEEM Objective) is operated at 10 kV with respect to the sample to accelerate low-energy electrons kicked out by the x rays. The XPEEM image is formed by photoelectrons emitted from the sample under the x-ray illumination. The inset shows the XPEEM image of the edge of the CuMnAs in the presence of SAWs, which are visible in the GaAs substrate as they modify the surface potential (however, no signal appears in the CuMnAs as it shunts the electrical signal and keeps the surface at a constant voltage).

In this paper, we generate Néel vector waves in collinear antiferromagnet CuMnAs induced by the time-dependent strain from the supporting GaAs substrate. We use stroboscopic x-ray photoemission electron microscopy combined with magnetic linear dichroism XMLD-PEEM to image both dynamic strain and Néel vector oscillations. We quantify both strain and amplitude of the Néel vector rotation up to $2.4°$. The overall amplitude of the observed Néel vector oscillations decreased with lowering temperature.

Experiments were carried out at the CIRCE beamline of the ALBA Synchrotron light source [30]. The CuMnAs epitaxial thin films with 45 nm thickness were grown on lattice-matched GaAs substrate by molecular beam epitaxy as described previously [31]. To generate SAWs with a frequency tuned to the synchrotron repetition rate (500 MHz), IDTs with a finger periodicity of 5.73 µm (which determines the SAW wavelength) were patterned and deposited on the GaAs by electron beam lithography and metal evaporation. The sample was mounted on a printed circuit board inside the sample holder and the IDT was contacted with wire bonds to apply electrical signals. The schematic illustration of the experiment is presented in Fig. 1. The radiofrequency signal applied to the IDT generates a SAW beam [32] traveling along the [110] crystalline direction of the GaAs substrate and confined to a depth in the order of the SAW wavelength [27]. The SAW causes a periodic in-plane, parallel to the SAW propagation direction, and out-of-plane change in the substrate lattice constant which is transferred as strain to the CuMnAs film.

In order to assess the structure of the CuMnAs thin film, x-ray diffraction (XRD) measurements were carried out on the sample using a laboratory diffractometer before the synchrotron experiment. The XRD pattern in Fig. 2(a) shows the peaks of both the CuMnAs film (black) and the GaAs substrate (red) with respect to 2θ. The tetragonal crystal system (P4/nmm) and the planes (001), (002), (003), and (004) of the antiferromagnetic thin film were identified with the

Powder Diffraction File 01-082-3986 from the Joint Committee on Powder Diffraction Standards-International Centre for Diffraction Data [33,34].

X-ray absorption spectroscopy (XAS) measurements of the CuMnAs were performed, detecting low-energy secondary electrons in the PEEM while scanning the photon energy. The beamline is equipped with an undulator that enables the control of the incoming x-ray polarization, for example,
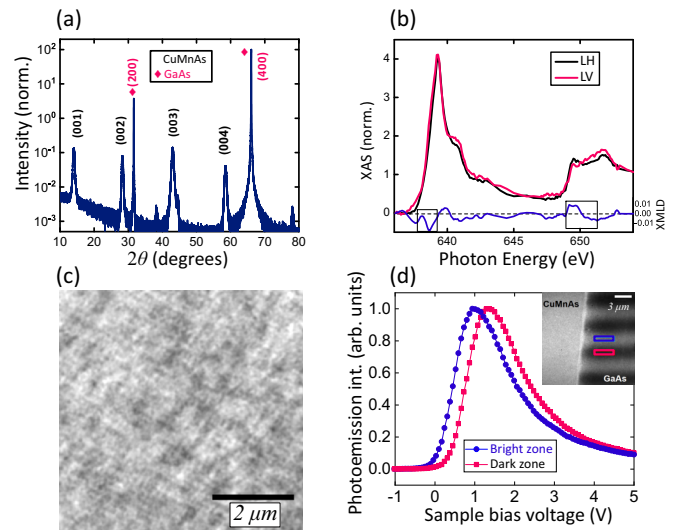

FIG. 2. (a) XRD measurements of 45 nm thin film of CuMnAs on GaAs showing the film (black) and substrate (red) peaks (b) XAS and XMLD spectra of CuMnAs/GaAs at the Mn $L_{3,2}$ edges, obtained with horizontal (black) and vertical (red) linear polarization. (c) An XMLD image of CuMnAs thin film at $T \simeq 223$ K without applying the SAW signal. The magnetic contrast is clearly visible in CuMnAs. (d) Quantification of the SAW: Average intensity (number of emitted electrons) from the red and blue rectangles in the inset as a function of sample bias voltage. The inset shows the XPEEM image of the SAW in GaAs (at the edge with CuMnAs) at 0.7 V bias.

between linear horizontal (electric field vector in the sample plane) and vertical (electric field vector under 16 degrees to the sample normal) polarization directions. X-ray absorption spectra at the Mn $L_{3,2}$ edges, with both polarizations, and their difference (linear dichroism, XMLD), are depicted in Fig. 2(b) at $T \simeq 235$ K. The features of the XMLD spectrum (blue line), marked by black boxes, are similar to previously published data [35].

The imaging of antiferromagnetic domains in the CuMnAs thin film is performed by XPEEM employing XMLD contrast. Such a contrast is obtained by subtracting different images taken with linear horizontal polarization at energies before and at the L_3 absorption peak (see details of the methodology in Supplemental Material [36] and also reference [37] therein). Figure 2(c) shows the domain arrangement in the film at 223 K nominal temperature without any SAWs applied. Equivalent images taken with linear vertical polarization (electric field vector $16°$ to the sample normal) did not show visible contrast, confirming a dominant in-plane Néel vector. In order to quantify the dynamic magnetoelastic effects in the CuMnAs film, it is necessary to determine first the amplitude of the SAW-induced strain. We cannot determine this quantity directly in the studied CuMnAs film because it is conductive and shunts the electrical component of the SAW, but instead, we can do it in the GaAs substrate. The inset of Fig. 2(d) depicts an XPEEM image of the sample surface in the presence of SAWs, measured with 500 MHz pulsed synchrotron x rays. An intensity contrast with a periodicity matching the SAW wavelength, i.e., 5.73 μm, is evident in the sample region not covered by the CuMnAs film. This contrast originates from the oscillating piezoelectric potential accompanying the strain wave at the surface of the GaAs substrate. The photoelectron spectra displayed in Fig. 2(d) show the average intensity (number of detected electrons) at the areas marked by the red and blue rectangles in the inset image, recorded as a function of the bias voltage applied to the substrate for a fixed energy analyzer configuration. The voltage shift between these curves, obtained by selecting the positions of maximum slope in both spectra, amounts to 0.35 V and corresponds to the peak-to-peak amplitude of the oscillating piezoelectric potential. This value is used to calculate the amplitude of the strain field by numerically solving the coupled differential equations of the mechanical and electrical displacement, obtaining values in the range of 0.01% at the sample surface. Details on stroboscopic XPEEM measurements with synchronized SAWs can be found in [11].

Figure 3 shows XMLD images at the CuMnAs taken while the SAW is applied. The bright and dark areas in Fig. 3 correspond to domains with spin axis parallel and perpendicular to the x-ray polarization, with a typical domain size below one micrometer. The presence of domains with continuously differing grayscale contrast indicates the absence of significant in-plane anisotropy for the spin axis in the sample. Between Fig. 3(a) and 3(b) the phase of the radiofrequency signal exciting the SAW was shifted by $180°$. Thus, the phase of the SAW in any given position is inverted for the stroboscopic measurement, i.e., when the x-rays hit the sample. A close inspection of the individual images shown in Figs. 3(a) and 3(b) as well as the difference image [Fig. 3(c)], same grayscale, does not show any observable change in the domain bound-
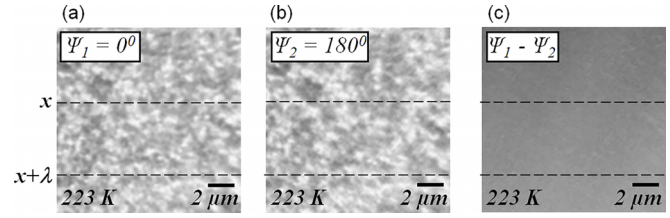

FIG. 3. XMLD images of CuMnAs with opposite electronic phases $\psi = 0°$ in (a) and $\psi = 180°$ in (b) of the SAW excitation at $T \simeq 223$ K. The direction of SAW propagation is perpendicular to the dashed lines which are separated by one wavelength of 5.73 μm. (c) Image obtained by subtracting the images at opposite phases, at the same contrast scale. No evident variations in the domain boundaries can be observed.

aries. The domain wall motion in the CuMnAs in the present experiment is thus either negligible or below the detection limit. The different images are used to eliminate the static domain contrast and enhance the dynamic changes induced by the SAW.

Several different images equivalent to the one shown in Fig. 3(c) were recorded at different SAW phases (typically $15°$) with a larger integration time to reduce noise. Figure 4(a) is a different image with a contrast enhanced about 100 times compared to Fig. 3(c) and shows the oscillatory component of the Néel vector. Line profiles along the direction of the SAW were extracted from each different image taken at different SAW phases. The results are summarized in Figs. 4(b)–4(d) and correspond to data sets at low temperatures, $T = 223$ K and $T = 233$ K, and room temperature, $T = 296$ K. The plotted curves correspond to the averaged profiles over all SAW phases (see Supplemental Material [36]
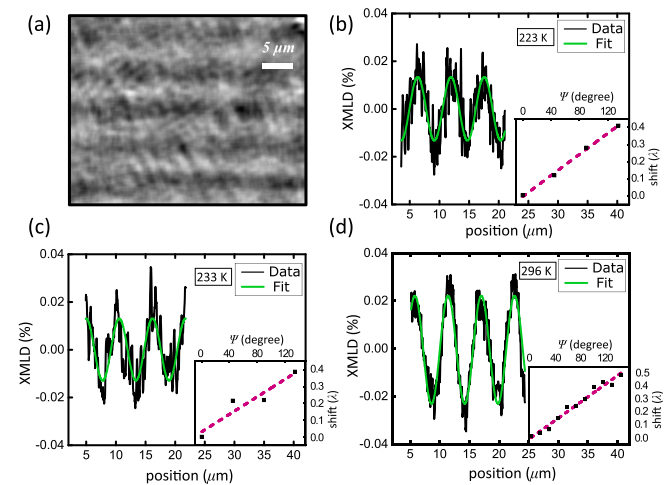

FIG. 4. Néel vector wave (spin axis rotation wave) in CuMnAs observed by XMLD-PEEM. (a) Image obtained by subtracting the XMLD images at opposite phases of SAW. (b)–(d) XMLD signal (in %) extracted from CuMnAs along the direction of the propagation of the SAW after averaging at $T \simeq 223$ K in (b), $T \simeq 233$ K, in (c) and $T \simeq 296$ K in (d). The black line in each plot shows the data and the green line is the sinusoidal function curve fitted to the data points. Insets show the fitted phase shift as a function of the shift ψ in the SAW excitation.

TABLE I. Quantitative results of the Néel vector wave in CuMnAs at different temperatures.

Temperature (K)	Max. XMLD domain dontrast ($\times 10^{-3}$)	SAW orientation w.r.t. x rays (degrees)	Strain amplitude ($\times 10^{-4}$)	XMLD wave amplitude ($\times 10^{-4}$)	Néel vector rotation (degrees)	Efficiency (degrees/strain $\times 10^{-4}$)
223	7.6 ± 1.0	65	0.86 ± 0.05	1.33	1.56 ± 0.21	1.81 ± 0.27
233	6.4 ± 1.0	65	0.86 ± 0.05	1.29	1.80 ± 0.29	2.09 ± 0.36
296	5.3 ± 0.7	90	0.75 ± 0.05	2.26	2.44 ± 0.33	3.26 ± 0.49

for details on the data analysis) and green lines are best fits with sinusoidal functions, which are used to obtain the amplitude of the Néel vector signal at each temperature. The insets of Figs. 4(b)–4(d) show the phase value from each different image profile, showing the measured shift of the wave in units of the wavelength, λ. These values are in excellent agreement with the electronic phase ψ applied to the IDT, which demonstrates that the Néel vector oscillations are driven by SAWs.

Now we turn to the quantitative analysis of the Néel vector rotation amplitudes for the three data sets at different temperatures, i.e., $T = 223$ K, $T = 233$ K, and $T = 296$ K. The results are summarized in Table I. Due to experimental constraints, the low-temperature data was taken with an angle of 65° between SAWs and probing x-rays, while room-temperature data was taken with a 90° angle. The conversion of XMLD amplitude to rotation in degrees, as well as the correction factor for the reduced sensitivity under 65°, is calculated in Supplemental Material [36]. As mentioned above, the applied strain from the SAW has been calculated from the voltage shift of the secondary electron spectra detected in the PEEM [Fig. 2(d)]. The typical strain amplitudes achieved in our experiments on GaAs are $(0.75 - 1) \times 10^{-4}$. The XMLD wave amplitude was determined from fits to the averaged line profiles in Figs. 4(b)–4(d). In order to convert those numbers into the corresponding rotation of the spin axis, we take first into account the temperature dependence of the XMLD contrast in CuMnAs. The XMLD wave amplitude is thus normalized to the maximum XMLD contrast for each temperature in the static domain image (see Fig. 2(c) for example), taken as average in three different locations each. We then consider the film to be populated by an equal portion of domains in all directions, i.e., without net in-plane anisotropy and calculate for each domain (i) the rotation angle as fraction of a maximum angle ϕ_0 as explained in Supplemental Material [36] and (ii) the sensitivity of the XMLD signal to this rotation as function of the domain spin axis.

The numbers reported in Table I show that the Néel vector wave driven by SAWs in CuMnAs can reach a sizable 2.44° at room temperature. We plotted in Fig. 5 the efficiency of the SAW-induced Néel vector wave defined as the overall variation divided by the SAW strain for the three temperatures. A similar quantity is added to the graph for magnetoacoustic waves in ferromagnetic samples measured through XMCD [22,38,39]. Values for ferromagnetic Ni [22] and Heusler alloy Fe$_3$Si [39] are shown as broad bands, because they depend on the external applied magnetic field, showing a resonance-like peak (Ni showed an efficiency of 2 to 4.5 and FeSi from 1.6 to 4.1). These results indicate a sizable dynamic magneto-elastic effect in CuMnAs induced by SAWs and a comparable efficiency like in FM materials. The space and time oscillating

strain results in a modulation of the film's anisotropy, which in an FM can be understood as a modulation of the effective magnetic field generating a modulation of the magnetic moment. However, in AFM such a small effective magnetic field does not serve to modulate magnetic moment or to shift magnetic domains but instead, it is capable of rotating the Néel vector with a similar efficiency. We notice here that the detection of spin axis rotation in CuMnAs is more challenging compared to magnetoacoustic waves in ferromagnets, mainly because the XMLD contrast is weaker and because the sample is in a multidomain state.

A reduction of the Néel vector wave excitation efficiency when lowering the temperature, i.e., from $3.3°/10^{-4}$ strain at room temperature (296 K) to $1.8°/10^{-4}$ at 223 K, has been observed. While this apparent reduction needs further experiments to be confirmed [40,41], it may indicate an increase of the energy barrier for the spin axis rotation as the temperature lowers (a type of "freezing"), or an increase of the Néel vector anisotropy value.

In summary, we have investigated high-frequency (500 MHz) magnetoelastic effects in antiferromagnetic CuMnAs excited by SAWs in the GaAs substrate using XMLD-PEEM. An averaged magnetoacoustic wave signal can be detected in XMLD, corresponding to a rotation of the spin axis in the individual domains by up to ±2.4°. The efficiency of the Néel vector excitation in CuMnAs is proof that magnetoelastic effects are a viable way to manipulate antiferromagnetic systems, even on the subnanosecond time scale. Moreover, in static conditions, the CuMnAs thin film
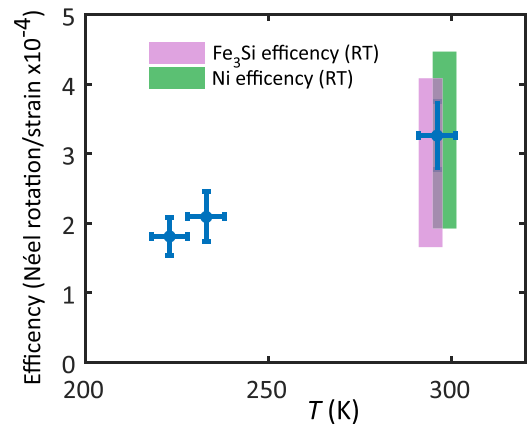

FIG. 5. Efficiency of the magnetoacoustic wave excitation in CuMnAs as a function of temperature in comparison with all data at 500 MHz SAW. The area for ferromagnetic samples corresponds to Ni and Fe$_3$Si at room temperature (RT) and covers the range between zero external field and resonance.

is characterized by a multidomain configuration of submicron size. No SAW-induced motion of domain walls has been detected, which could be related to intrinsic pinning due to the film microstructure. In the future, a combination of GaP substrates with ZnO-based IDT can enable to study SAW-driven effects in high-quality single domain patterns of CuMnAs.

[1] A. A. Sapozhnik, M. Filianina, S. Y. Bodnar, A. Lamirand, M.-A. Mawass, Y. Skourski, H.-J. Elmers, H. Zabel, M. Kläui, and M. Jourdan, Direct imaging of antiferromagnetic domains in Mn_2Au manipulated by high magnetic fields, Phys. Rev. B **97**, 134429 (2018).

[2] P. Wadley, B. Howells, J. Železný, C. Andrews, V. Hills, R. P. Campion, V. Novák, K. Olejnik, F. Maccherozzi, S. S. Dhesi *et al.*, Electrical switching of an antiferromagnet, Science **351**, 587 (2016).

[3] H. Meer, F. Schreiber, C. Schmitt, R. Ramos, E. Saitoh, O. Gomonay, J. Sinova, L. Baldrati, and M. Kläui, Direct imaging of current-induced antiferromagnetic switching revealing a pure thermomagnetoelastic switching mechanism in NiO, Nano Lett. **21**, 114 (2021).

[4] P. Wadley, S. Reimers, M. J. Grzybowski, C. Andrews, M. Wang, J. S. Chauhan, B. L. Gallagher, R. P. Campion, K. W. Edmonds, S. S. Dhesi *et al.*, Current polarity-dependent manipulation of antiferromagnetic domains, Nat. Nanotechnol. **13**, 362 (2018).

[5] T. Janda, J. Godinho, T. Ostatnicky, E. Pfitzner, G. Ulrich, A. Hoehl, S. Reimers, Z. Soban, T. Metzger, H. Reichlova *et al.*, Magneto-seebeck microscopy of domain switching in collinear antiferromagnet CuMnAs, Phys. Rev. Mater. **4**, 094413 (2020).

[6] S. Reimers, D. Kriegner, O. Gomonay, D. Carbone, F. Krizek, V. Novák, R. P. Campion, F. Maccherozzi, A. Björling, O. J. Amin *et al.*, Defect-driven antiferromagnetic domain walls in CuMnAs films, Nat. Commun. **13**, 724 (2022).

[7] I. Fina and J. Fontcuberta, Strain and voltage control of magnetic and electric properties of FeRh films, J. Phys. D: Appl. Phys. **53**, 023002 (2020).

[8] B.-Y. Wang, C.-H. Hsiao, B.-X. Liao, C.-Y. Hsu, T.-H. Li, Y.-L. Hsu, Y.-M. Lai, M.-S. Tsai, T.-H. Chuang, and D.-H. Wei, Perpendicular magnetic anisotropy induced by nimn-based antiferromagnetic films with in-plane spin orientations: Roles of interfacial and volume antiferromagnetic moments, Phys. Rev. B **104**, 024424 (2021).

[9] H. Meer, O. Gomonay, C. Schmitt, R. Ramos, L. Schnitzspan, F. Kronast, M.-A. Mawass, S. Valencia, E. Saitoh, J. Sinova *et al.*, Strain-induced shape anisotropy in antiferromagnetic structures, Phys. Rev. B **106**, 094430 (2022).

[10] J. A. Arregi, F. Ringe, J. Hajduček, O. Gomonay, T. Molnár, J. Jaskowiec, and V. Uhlíř, Magnetic-field-controlled growth of magnetoelastic phase domains in ferh, J. Phys.: Mater. **6**, 034003 (2023).

[11] M. Foerster, N. Statuto, B. Casals, A. Hernández-Mínguez, R. Cichelero, P. Manshausen, A. Mandziak, L. Aballe, J. Hernández Ferràs, and F. Macià, Quantification of propagating and standing surface acoustic waves by stroboscopic X-ray photoemission electron microscopy, J. Synchrotron Radiat. **26**, 184 (2019).

[12] J. Hernandez, P. Santos, F. Macià, A. García-Santiago, and J. Tejada, Acoustomagnetic pulse experiments in $LiNbO_3/Mn_{12}$ hybrids, Appl. Phys. Lett. **88**, 012503 (2006).

[13] S. Davis, A. Baruth, and S. Adenwalla, Magnetization dynamics triggered by surface acoustic waves, Appl. Phys. Lett. **97**, 232507 (2010).

[14] M. Weiler, L. Dreher, C. Heeg, H. Huebl, R. Gross, M. S. Brandt, and S. T. B. Goennenwein, Elastically driven ferromagnetic resonance in nickel thin films, Phys. Rev. Lett. **106**, 117601 (2011).

[15] M. Weiler, H. Huebl, F. S. Goerg, F. D. Czeschka, R. Gross, and S. T. B. Goennenwein, Spin pumping with coherent elastic waves, Phys. Rev. Lett. **108**, 176601 (2012).

[16] L. Thevenard, I. S. Camara, S. Majrab, M. Bernard, P. Rovillain, A. Lemaître, C. Gourdon, and J.-Y. Duquesne, Precessional magnetization switching by a surface acoustic wave, Phys. Rev. B **93**, 134430 (2016).

[17] D. Labanowski, A. Jung, and S. Salahuddin, Power absorption in acoustically driven ferromagnetic resonance, Appl. Phys. Lett. **108**, 022905 (2016).

[18] M. Foerster, F. Macià, N. Statuto, S. Finizio, A. Hernández-Mínguez, S. Lendínez, P. V. Santos, J. Fontcuberta, J. M. Hernàndez, M. Kläui *et al.*, Direct imaging of delayed magneto-dynamic modes induced by surface acoustic waves, Nat. Commun. **8**, 407 (2017).

[19] P. Kuszewski, I. S. Camara, N. Biarrotte, L. Becerra, J. von Bardeleben, W. S. Torres, A. Lemaître, C. Gourdon, J.-Y. Duquesne, and L. Thevenard, Resonant magneto-acoustic switching: influence of rayleigh wave frequency and wavevector, J. Phys.: Condens. Matter **30**, 244003 (2018).

[20] M. Foerster, L. Aballe, J. M. Hernàndez, and F. Macià, Subnanosecond magnetization dynamics driven by strain waves, MRS Bull. **43**, 854 (2018).

[21] A. Adhikari and S. Adenwalla, Surface acoustic waves increase magnetic domain wall velocity, AIP Adv. **11**, 015234 (2021).

[22] B. Casals, N. Statuto, M. Foerster, A. Hernández-Mínguez, R. Cichelero, P. Manshausen, A. Mandziak, L. Aballe, J. M. Hernàndez, and F. Macià, Generation and imaging of magnetoacoustic waves over millimeter distances, Phys. Rev. Lett. **124**, 137202 (2020).

[23] C. Müller, P. Durdaut, R. B. Holländer, A. Kittmann, V. Schell, D. Meyners, M. Höft, E. Quandt, and J. McCord, Imaging of love waves and their interaction with magnetic domain walls in magnetoelectric magnetic field sensors, Adv. Electron. Mater. **8**, 2200033 (2022).

[24] K. M. Seemann, O. Gomonay, Y. Mokrousov, A. Hörner, S. Valencia, P. Klamser, F. Kronast, A. Erb, A. T. Hindmarch, A. Wixforth, C. H. Marrows, and P. Fischer, Magnetoelastic resonance as a probe for exchange springs at antiferromagnet-ferromagnet interfaces, Phys. Rev. B **105**, 144432 (2022).

[25] P. Delsing, A. N. Cleland, M. J. A. Schuetz, J. Knörzer, G. Giedke, J. I. Cirac, K. Srinivasan, M. Wu *et al.*, The 2019 surface acoustic waves roadmap, J. Phys. D **52**, 353001 (2019).

[26] W.-G. Yang and H. Schmidt, Acoustic control of magnetism toward energy-efficient applications, Appl. Phys. Rev. **8**, 021304 (2021).

[27] J. Puebla, Y. Hwang, S. Maekawa, and Y. Otani, Perspectives on spintronics with surface acoustic waves, Appl. Phys. Lett. **120**, 220502 (2022).

[28] B. Dong and M. E. Zaghloul, Generation and enhancement of surface acoustic waves on highly doped p-type GaAs substrate, Nanoscale Adv. **1**, 3537 (2019).

[29] A. Rampal and R. N. Kleiman, Optical actuation of a micromechanical photodiode via the photovoltaic-piezoelectric effect, Microsyst. Nanoeng. **7**, 29 (2021).

[30] L. Aballe, M. Foerster, E. Pellegrin, J. Nicolas, and S. Ferrer, The ALBA spectroscopic LEEM-PEEM experimental station: layout and performance, J. Synchrotron Radiat. **22**, 745 (2015).

[31] P. Wadley, V. Novák, R. P. Campion, C. Rinaldi, X. Marti, H. Reichlová, J. Železný, J. Gázquez, M. A. Roldan, M. Varela, D. D. Khalyavin, S. Langridge, D. Kriegner, F. Máca, J. D. I. Masek, R. Bertacco, V. Holý, A. W. Rushforth, K. W. Edmonds, B. L. Gallagher *et al.*, Tetragonal phase of epitaxial room-temperature antiferromagnet CuMnAs, Nat. Commun. **4**, 2322 (2013).

[32] B. von Boehn, M. Foerster, M. von Boehn, J. Prat, F. Macià, B. Casals, M. Khaliq, A. Hernández-Mínguez, L. Aballe, and R. Imbihl, On the promotion of catalytic reactions by surface acoustic waves, Angew. Chem. Int. Ed. **59**, 20224 (2020).

[33] A. N. Nateprov, V. C. Kravtsov, V. Fritsch, and H. von Löhneysen, Structure and properties of the tetragonal phase of MnCuAs, Surf. Engin. Appl. Electrochem. **47**, 540 (2011).

[34] V. Hills, P. Wadley, R. P. Campion, R. Beardsley, K. W. Edmonds, B. L. Gallagher, V. Novak, B. Ouladdiaf, and T. Jungwirth, Paramagnetic to antiferromagnetic transition in epitaxial tetragonal CuMnAs, J. Appl. Phys. **117**, 172608 (2015).

[35] P. Wadley, V. Hills, M. Shahedkhah, K. Edmonds, R. Campion, V. Novák, B. Ouladdiaf, D. Khalyavin, S. Langridge, V. Saidl, P. Nemec, A. Rushforth, B. Gallagher, S. Dhesi, F. Maccherozzi, J. Železný, and T. Jungwirth, Antiferromagnetic structure in tetragonal CuMnAs thin films, Sci. Rep. **5**, 17079 (2015).

[36] See Supplemental Material at http://link.aps.org/supplemental/10.1103/PhysRevMaterials.8.084406 for (I) Imaging domains description; (II) details on the data analysis and imaging of Néel vactor waves; and (III) the modelling of the Néel vector wave and quantification of the rotation angle.

[37] M. J. Grzybowski, P. Wadley, K. W. Edmonds, R. Beardsley, V. Hills, R. P. Campion, B. L. Gallagher, J. S. Chauhan, V. Novak, T. Jungwirth, F. Maccherozzi, and S. S. Dhesi, Imaging current-induced switching of antiferromagnetic domains in cumnas, Phys. Rev. Lett. **118**, 057701 (2017).

[38] M. Rovirola, M. Waqas Khaliq, T. Gustafson, F. Sosa-Barth, B, Casals, J. M. Hernández, S. Ruiz-Gómez, M. A. Niño, L. Aballe, A. Hernández-Mínguez, M. Foerster, and F. Macià, Study of the magnetoelastic effect in nickel and cobalt thin films at GHz range using x-ray microscopy, Phys. Rev. Res. **6**, 023285 (2024).

[39] M. Rovirola, M. W. Khaliq, B. Casals, M. Foerster, M. A. Niño, J. Herfort, J. M. Hernàndez, F. Macià, and A. Hernández-Mínguez, Resonant and off-resonant magnetoacoustic waves in epitaxial Fe_3Si/GaAs hybrid structures, Phys. Rev. Appl. **20**, 034052 (2023).

[40] V. Grigorev, M. Filianina, Y. Lytvynenko, S. Sobolev, A. R. Pokharel, A. P. Lanz, A. Sapozhnik, A. Kleibert, S. Y. Bodnar, P. Grigorev, Y. Skourski, M. Kläui, H.-J. Elmers, M. Jourdan, and J. Demsar, Optically-triggered strain-driven Néel vector manipulation in a metallic antiferromagnet, ACS Nano **16**, 20589 (2022).

[41] T. P. Lyons, J. Puebla, K. Yamamoto, R. S. Deacon, Y. Hwang, K. Ishibashi, S. Maekawa, and Y. Otani, Acoustically driven magnon-phonon coupling in a layered antiferromagnet, Phys. Rev. Lett. **131**, 196701 (2023).